The Astrophysical Journal Letters, 971:L43 (6pp), 2024 August 20 https://doi.org/10.3847/2041-8213/ad6660

PO and PN in the Envelope of VY Canis Majoris: Elucidating the Chemistry and Origin of Phosphorus

R. Ravi[1], A. P. Singh[1], A. M. S. Richards[2], R. M. Humphreys[3], L. Decin[4], and L. M. Ziurys[1,5]
[1] Department of Chemistry and Biochemistry, University of Arizona, USA; lziurys@email.arizona.edu
[2] Department of Astronomy, University of Manchester, UK
[3] Minnesota Institute for Astrophysics, University of Minnesota, USA
[4] Institute of Astronomy, Department of Physics and Astronomy, KU. Leuven, Belgium
[5] Department of Astronomy, Steward Observatory, University of Arizona, USA

Received 2023 December 02; revised 2024 July 17; accepted 2024 July 22; published 2024 August 17

Abstract

The $J = 5.5 \rightarrow 4.5$ and $J = 5 \rightarrow 4$ transitions of PO and PN, respectively, have been imaged in the envelope of hypergiant star VY Canis Majoris (VY CMa) using the Atacama Large Millimeter/submillimeter Array with angular resolutions of $0\farcs2$ and $1\farcs5$ and data from the Submillimeter Telescope of the Arizona Radio Observatory. These maps are the first high-fidelity images of PO and PN in a circumstellar envelope. Both molecules are primarily present in a spherical, star-centered region with a radius $\sim 60\,R_*$ ($0\farcs5$), indicating formation by LTE chemistry and then condensation into grains. PN, however, shows additional, fan-shaped emission $2''$ southwest of the star, coincident with dust features resolved by Hubble Space Telescope (HST), as well as four newly identified distinct structures $1''$–$2''$ toward the north, east, and west (Cloudlets I–IV), not visible in HST images. The "SW Fan" and the cloudlets are also prominent in the $J = 5.5 \rightarrow 4.5$ transition of NS. The correlation of PN with NS, SiO, and dust knots in the SW Fan suggests a formation in shocked gas enhanced with nitrogen. Excess nitrogen is predicted to favor PN synthesis over PO. Abundances for PN and PO in the spherical source are $f \sim 4.4 \times 10^{-8}$ and 1.4×10^{-7}, respectively, relative to H_2. Given a cosmic abundance of phosphorus, an unusually high fraction ($\sim$35%) is contained in PO and PN. Alternatively, the stellar winds may be enriched in P (and N) by dredge-up from the interior of VY CMa.

Unified Astronomy Thesaurus concepts: Astrochemistry (75); Interstellar molecules (849); Chemical abundances (224); Hypergiant stars (774); Millimeter astronomy (1061); Circumstellar envelopes (237)

1. Introduction

Although phosphorus has a relatively low cosmic abundance (Asplund et al. 2009), it plays an important role in astrobiology as one of the six "NCHOPS" elements deemed necessary for life (e.g., Bernal et al. 2021). Phosphorus is also thought to be critical in the formation of cores of Earth-like planets, as the mineral schreibersite, (Fe, Ni)$_3$P (Hinkel et al. 2020). This material is calculated to be the most thermodynamically stable form of phosphorus in a mixture of near-solar composition (e.g., Lodders and Fegley 1999). Phosphorus, however, has been an elusive element. Its atomic transitions lie in unfavorable regions of the electromagnetic spectrum (e.g., Roederer et al. 2014; Maas et al. 2022), limiting observations (Hinkel et al. 2020; Koelemay et al. 2023). Furthermore, its origin is uncertain. Phosphorus is thought to be formed by neutron capture processes in massive ($>10\,M_\odot$) stars and subsequently released into the interstellar medium (ISM) by Type II supernova (SN) explosions (e.g., Caffau et al. 2011). SN yields, however, fall short of reproducing the observed abundances (Cescutti et al. 2012; Nandakumar et al. 2022), suggesting there are other stellar sources of phosphorus (Karakas 2010).

Seven phosphorus-bearing molecules, alternative probes of this element, have been securely identified in interstellar gas: PN, PO, CP, CCP, HCP, PH$_3$, and SiP (Milam et al. 2008; Ziurys et al. 2018; Koelemay et al. 2022). These species have principally been detected in circumstellar envelopes of evolved stars. PN and PO, however, have been observed in molecular clouds, where they may be associated with shocks (e.g., Ziurys 1987; Fontani et al. 2019; Rivilla et al. 2020; Bernal et al. 2021). Abundances of phosphorus-containing molecules, relative to H_2, are higher in circumstellar envelopes, with $f(X/H_2) \sim 10^{-9}$–10^{-7} (Kamiński et al. 2013), than in molecular clouds, where PO and PN have values $f(X/H_2) \sim 10^{-11}$–10^{-10} (Ziurys 2024).

One of the first circumstellar sources where phosphorus-bearing molecules have been identified is the envelope of VY Canis Majoris (VY CMa). VY CMa is a massive ($\sim 40\,M_\odot$, $R_* = 1.4 \times 10^{14}$ cm), luminous ($5 \times 10^5\,L_\odot$) hypergiant star located at a distance of 1140 pc, with a mass loss rate of $\sim 2 \times 10^{-4}\,M_\odot\,\mathrm{yr}^{-1}$ (Decin et al. 2006; Shenoy et al. 2016; Dinh-V-Trung et al. 2022). The mass loss is sporadic and highly directional, creating an irregular envelope composed of numerous clumps, knots, and arcs, seen in Hubble Space Telescope (HST) images of scattered starlight (e.g., Humphreys et al. 2007, 2021) and in molecular outflows (e.g., Ziurys et al. 2007; Tenenbaum et al. 2010; Kamiński et al. 2013). The most prominent collimated outflows are the NW Arc, the NE Arc, Arc 1, and Arc 2 (Singh et al. 2023), which extend as far as $9''$ from the stellar position. There is also a roughly spherical flow close to the star, seen in PO and PN, tracing the overall mass loss (Tenenbaum et al. 2007, 2010; Kamiński et al. 2013).

To further examine circumstellar phosphorus, the $J = 5.5 \rightarrow 4.5$ lambda-doublets of PO and the $J = 5 \rightarrow 4$ line of PN have been imaged in the envelope of VY CMa at 1 mm, using

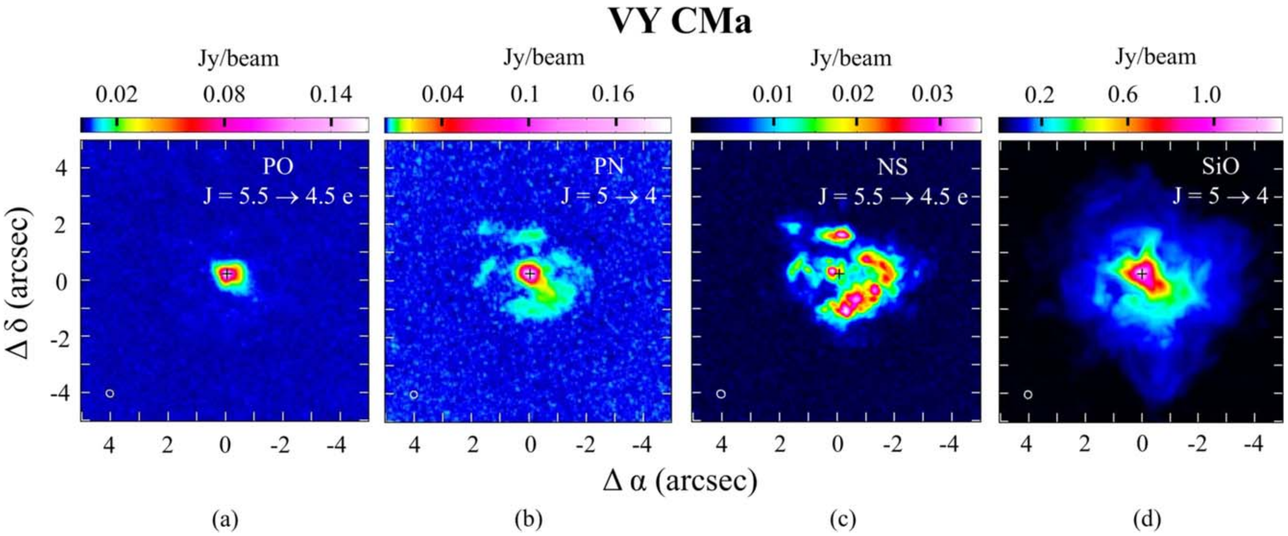

Figure 1. Combined moment 8 ALMA and SMT images of $J = 5.5 \rightarrow 4.5$ *e* transition of PO (left, a), $J = 5 \rightarrow 4$ transition of PN (left, b), $J = 5.5 \rightarrow 4.5$ *e* transition of NS (right, c), $J = 5 \rightarrow 4$ transition of SiO (right, d). Synthesized beam sizes are shown at the lower left, crosses indicate the stellar position. Flux scale (Jy beam^{-1}) is indicated in the figure. The axes are in arcseconds relative to the (0, 0) position corresponding to $\alpha = 07^{\rm h}22^{\rm m}58^{\rm s}.33$, $\delta = -25^\circ46'03''.2$ (J2000.0 ICRS). PN is clearly more extended than PO, with a close correspondence to NS and partly to SiO.

Atacama Large Millimeter/submillimeter Array (ALMA) with resolutions $0''.2$ and $1''.5$. These data have been combined with previous single-dish spectra from the Arizona Radio Observatory (ARO) Submillimeter Telescope (SMT) to produce the first high-fidelity images of these molecules. In this Letter, we present these results and discuss their implications for chemistry and nucleosynthesis.

2. Observations

The 1 mm transitions of PO and PN were observed toward VY CMa using ALMA at Band 6 for the project 2021.1.01054. S between 2021 December and 2022 June. These data are part of a set of observations covering molecular lines between 216.0 and 269.3 GHz, and comprise a third paper of an ongoing series (Singh et al. 2023; Humphreys et al. 2024). The observations and data processing are described in Singh et al. (2023). In summary, to recover all the flux, data from two ALMA configurations were combined with spectra taken using the ARO SMT (Tenenbaum et al. 2010). The image cubes presented here have angular resolutions of $0''.2$ and $1''.5$ and maximum recoverable scales of $11''$, with off-source rms noise per channel <1 mJy. The astrometric accuracy is better than 30 mas and the absolute flux scale accuracy is ~10% or better. Continuum images made from all line-free data were used to identify the stellar position and register all data to within a few milliarcseconds. The position measured for VY CMa was $\alpha = 07^{\rm h}22^{\rm m}58^{\rm s}.32$, $\delta = -25^\circ46'03''.01$ (J2000 ICRS; Singh et al. 2023). Velocities are in the kinematic local standard of rest convention (LSR) relative to the rest frequency of the given line, assuming $V_{\rm LSR} = 20.0$ km s^{-1} for the star, based on CO spectra.

The transition frequencies used for PO were 239953.5 MHz and 240146.8 MHz ($J = 5.5 \rightarrow 4.5$ *e* and *f*) and 234935.7 MHz for PN ($J = 5 \rightarrow 4$). The $J = 5.5 \rightarrow 4.5$ *e* transition of NS at 253571.0 GHz and the $J = 5 \rightarrow 4$ ($v = 0$) line of SiO at 217104.9 MHz were also measured. The derived ALMA images are presented as moment 8 (peak intensity) maps. For PO and PN, the rms of the moment 8 images were ~3 mJy and ~2 mJy with a signal-to-noise ratio (S/N) of 49.6 and 99.2, respectively. The SiO and NS images had rms values of ~4 mJy and ~2 mJy with S/N of 342 and 17.5. The conversion factor from Jy beam^{-1} to brightness temperature $T_{\rm R}$ (K) is 343 and 385 at 239.9 GHz ($\theta_{\rm b} \sim 0''.27$) and 217.1 GHz ($\theta_{\rm b} \sim 0''.25$).

3. Results

Composite (moment 8) images for PO, $J = 5.5 \rightarrow 4.5$ *e* and PN, $J = 5 \rightarrow 4$ lines are shown in Figure 1 (left panels), with their intensity scales. The position of the star is marked by a cross. The matching lambda doublet in PO is not shown because it is contaminated by Na^{37}Cl ($v = 1$).

As illustrated in the figure, the emission of PO is confined to within $0.5''$ of the star, or 60 R_*, in a roughly circular shape, with some slight asymmetry in the east–west direction and a small elongation to the southwest. PN emission has almost an identical distribution with a similar elongation. This spherical source was recognized in the line profiles of earlier single-dish observations (e.g., Tenenbaum et al. 2010). However, PN also has weaker emission reaching $1''.5$ to the southwest, present in an outflow resembling a "fan" structure about $2''$ across. The "SW Fan" appears to encompass several knots observed in HST images (Humphreys et al. 2021). There are also four other separate, lower intensity clumps ~ $1''.25$–$2''$ to the east, west, and northeast of the star (Cloudlets I–IV). PO is not present in any of these structures. HCN is visible in Cloudlets III and IV and in the SW Fan as well (Singh et al. 2023). Note that the dipole moments of PO and PN are similar (1.88 D versus 2.75 D).

Also shown in Figure 1 (two right panels) are composite (moment 8) images for NS, $J = 5.5 \rightarrow 4.5$ *e* and SiO, $J = 5 \rightarrow 4$ lines. These data will be discussed in a future paper. NS (dipole moment: 1.81 D) is very prominent in the SW Fan and the four cloudlets and shows a remarkable similarity to PN. SiO emission is clearly present in the SW Fan but not in the cloudlets, although it traces other structures.

Figure 2 displays ALMA spectra obtained for PO ($J = 5.5 \rightarrow 4.5$, *e* and *f*) and PN ($J = 5 \rightarrow 4$), created from the spherical regions shown in Figure 1. The two lambda-

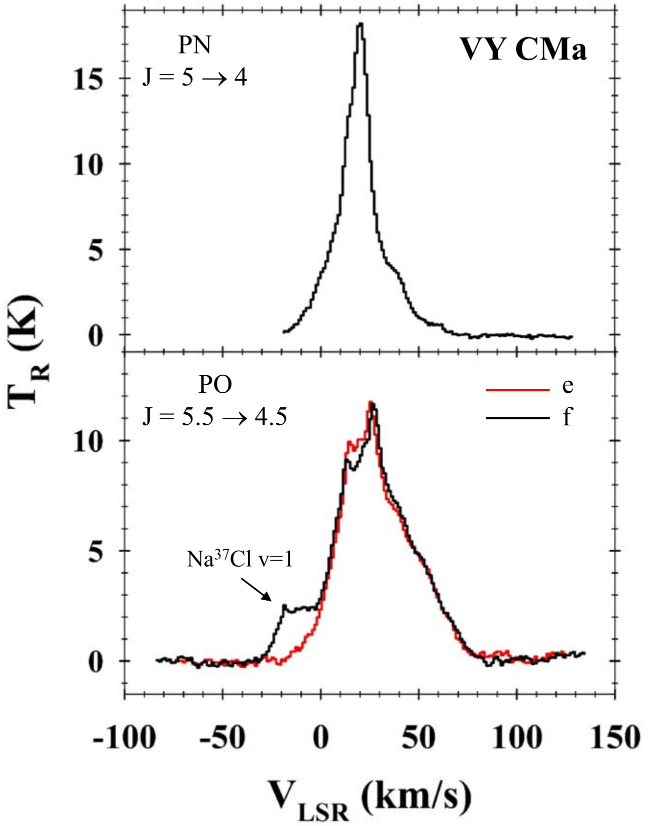

Figure 2. Spectra arising from the spherical flow of the $J = 5 \rightarrow 4$ transition of PN (upper) and the $J = 5.5 \rightarrow 4.5$ *e* (in red), *f* (in black) transition of PO (lower). The presence of phosphorus hyperfine structure broadens the PO line profile relative to that of PN.

doublets of the $J = 5.5 \rightarrow 4.5$ transition of PO are overlaid, with *e* in red and *f* in black. Note that the *f* line has a weak, blue-shifted “shoulder” arising from the $J = 19 \rightarrow 18$ transition of $Na^{37}Cl$, $v = 1$. The PO line appears broader than that of PN with $\Delta V_{1/2} \sim 37$ km s^{-1} (full width at half-maximum intensity) with two closely spaced emission peaks ($V_{LSR} \sim 14$ and 26 km s^{-1}). These two features arise from phosphorus hyperfine doublets, separated by 9–11 MHz or 12–14 km s^{-1}, which broadens the line profile. The PN linewidth is $\Delta V_{1/2} \sim 22$ km s^{-1}. The LSR velocity for both lines is $V_{LSR} \sim 20$–21 km s^{-1}, the systemic velocity of the star. The similarity of line profiles indicates that both molecules arise from the same material.

Figure 3 compares the distribution of PN relative to NS and the HST optical image. In Figure 3(a) (left), the image of NS is shown with the PN emission (black contours) from Figure 1. PN emission closely traces that of NS in both the SW Fan and the four cloudlets, although the latter molecule is ∼2–3 times brighter. Furthermore, the line profiles of the two molecules are virtually identical in shape in these regions, as shown in Figure 3(c) (right: NS: red, PN: black). All five main velocity components of the SW Fan are observed in both molecules, as well as the features of the cloudlets. Note that nitrogen hyperfine interactions slightly broaden the NS profiles. Figure 3(b) (center) shows the HST image (grayscale) from Humphreys et al. (2021), overlaid with the same PN contours (red). PN appears to encompass the main SW and S dust knots, labeled on the figure. Moreover, the velocities agree between PN and KI emission (Humphreys et al. 2021) for several of the features.

Table 1 lists the major emission features for PO and PN, their approximate positions, and line parameters (V_{LSR}, $\Delta V_{1/2}$, and peak intensity). The HST dust features that match in LSR velocity and position with PN are also listed in the table, which includes S Knot B (10.4 km s^{-1}), SW Knot A (20.4 km s^{-1}), and S Knot E1/S Knot E2/SW Knot G (37.9 km s^{-1}), see Humphreys et al. (2021). There is no current match for the -4.5 km s^{-1} or tentative ∼28 km s^{-1} component.

Selected spectra (Table 1) were modeled with the non–local thermodynamic equilibrium (LTE) radiative transfer code ESCAPADE (Adande et al. 2013; Singh et al. 2021, 2022). The code, based on the Sobolev approximation, employs the escape probability formalism, considering collisional and infrared excitation, as typical for circumstellar radiative transfer calculations. Radial temperature and density profiles are assumed for the modeling, taken from the detailed work of Zubko et al. (2004) and Decin et al. (2006). We estimate that the maximum uncertainties arising from these profiles are 10% (temperature) and 30% (density). The code was used to model the molecular abundance of PO and PN in the spherical and SW Fan outflows. The SW Fan required an asymmetric wind (cone) approximation: see Singh et al. (2021). The best fit for the spherical flow for both PO and PN suggests a source size of $\sim 60\,R_*$, supported by the ALMA images, starting the calculation at $5\,R_*$. For the SW Fan, the abundance reaches a maximum at $\sim 60\,R_*$ with a source size extending to $\sim 120\,R_*$. Derived PO and PN abundances, with respect to H_2, are given in Table 2. Estimated abundance uncertainties are 35%.

4. Discussion

4.1. The Chemistry of PO and PN in the Spherical Outflow in VY CMa

The fractional abundances of PO and PN in the spherical source in the envelope of VY CMa are $f = 1.4\ (0.5) \times 10^{-7}$ and $4.4\ (1.5) \times 10^{-8}$, respectively, relative to H_2. The SW Fan exhibits PN abundance of $f = 2.6\ (0.9) \times 10^{-8}$, with the four additional clumps each having $f = 0.2$–0.5×10^{-8}. These abundances are in reasonable agreement with those modeled by Ziurys et al. (2018), who found $f \sim 5 \times 10^{-8}$ and $\sim 10^{-8}$ for PO and PN, respectively, based on ARO SMT spectra.

The abundance of PO estimated for another hypergiant star, NML Cyg, is comparable at $f \sim 7 \times 10^{-8}$ (Ziurys et al. 2018), although that of PN was significantly lower ($f \sim 0.3 \times 10^{-8}$). However, these values are based on single-dish spectra. For the envelopes of the O-rich asymptotic giant branch stars IK Tau, TX Cam, and R Cas, $PN/H_2 \sim 1$–2×10^{-8} and $PO/H_2 \sim 0.5$–1×10^{-7} (De Beck et al. 2013; Ziurys et al. 2018). VY CMa has the highest abundances of both molecules, but all circumstellar shells follow the chemical trend that $f(PO) > f(PN)$. This pattern is also observed in star-forming regions, where $f(PO) > f(PN)$, but abundances are considerably lower ($f \sim 10^{-11}$–10^{-10}; Bernal et al. 2021).

PO emission is exclusively centered on the star, which is also the main concentration of PN. These distributions suggest that both molecules are formed close to the photosphere. In this region, the gas is sufficiently hot and dense that chemical reactions occur under conditions of LTE and therefore are path-independent (i.e., favored products have the lowest relative Gibbs free energy; Glassgold 1996; Agúndez et al. 2007;

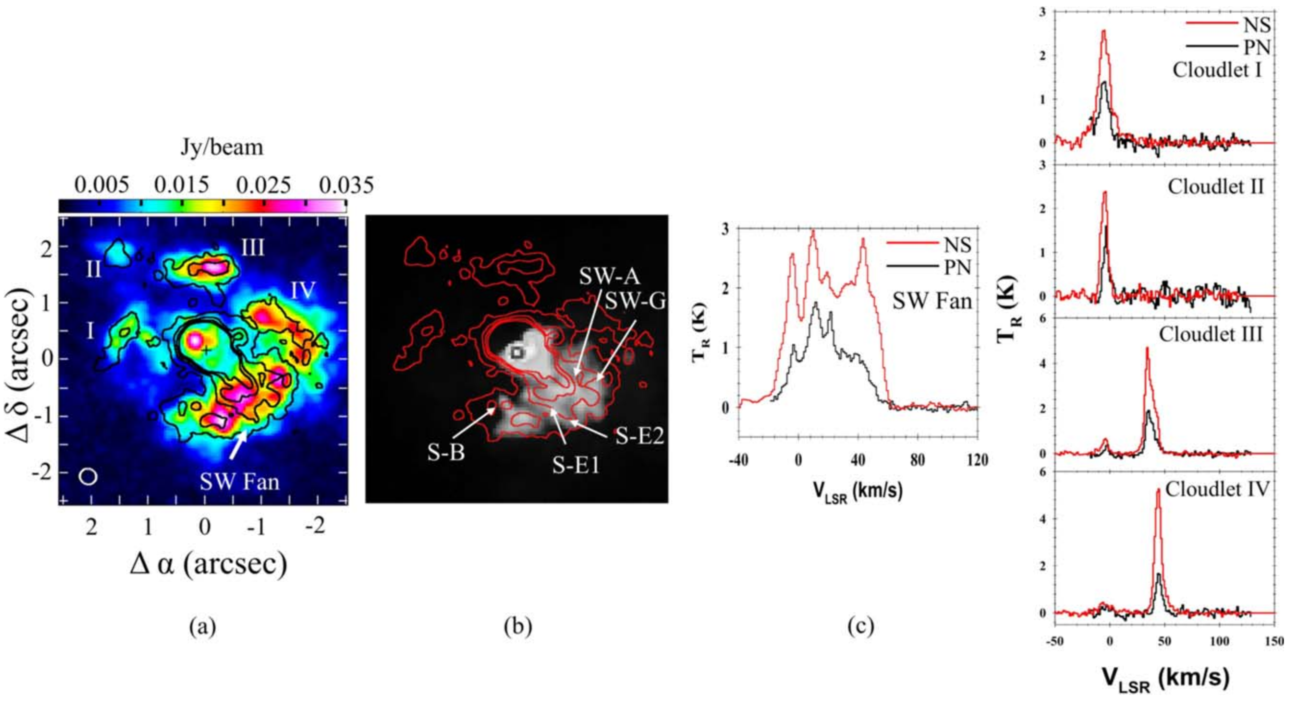

(a) (b) (c)

Figure 3. Emission contours of PN superimposed over (a) the image of NS from Figure 1 (in black) and (b) the HST F656N (6563.7 Å) image (in red) from Humphreys et al. (2021). The axes are defined as in Figure 1. The SW Fan, Cloudlets I–IV, and certain HST dust features are indicated. PN emission coincides with NS and some of the dust clumps, including South Knots B, E1 and E2, and SW Knots A and G (see Table 1). Spectra of PN (black) and NS (red) for the SW Fan and the cloudlets are shown in (c), plotted on the same velocity scale.

Ziurys et al. 2016). LTE models of inner envelope chemistry in O-rich stars predict that PO is more abundant than PN in the temperature range approximately 1000–2300 K (Tsuji 1973; Milam et al. 2008). PO attains a peak abundance of $f \sim 10^{-7}$ near $T \sim 1500$ K, which is consistent with the observed abundance and the photospheric temperature of ∼3000–3500 K (Wittkowski et al. 2012). The predicted PN abundance at 1500 K is $f \sim 10^{-9}$—a factor of 14 lower than observed ($f \sim 4.4 \times 10^{-8}$). However, as noted by Lodders (2004), there is disagreement in the thermodynamic data for PN. Furthermore, the model predicts a very high abundance of PS at 1500 K—near 10^{-7}. PS has yet to be detected, despite sensitive searches. If the phosphorus predicted to be in PS were partly channeled into PN, then the agreement would be improved.

After LTE formation, PO and PN disappear at $r \sim 60\,R_*$, a likely result of condensation into grains. It is not an excitation effect, as physical conditions at this radius are favorable for the population of rotational levels ($T \sim 300$ K, $n \sim 10^6$–10^7 cm^{-3}). Dust continuum emission around VY CMa, although asymmetric, extends out as far as 60 R_*, consistent with this scenario (O'Gorman et al. 2015).

4.2. The Unusual Presence of PN in Extended Material

While PO is confined to the inner circumstellar envelope, PN appears in other structures 1.″5–2″ (180–240 R_*) from the star. These distances are well beyond the LTE chemical region. The close association of the velocities of PN emission with those of KI in the SW and S clumps suggests that the formation is related to the mass ejections that created these structures, which occurred 200–300 yr ago (Humphreys et al. 2021) and generated highly shocked material. Therefore, a possible formation scenario is that the ejected mass impacted phosphorus-containing grains, liberating the element to create PN. Evidence for the shock scenario is the noticeable similarity between PN and SiO emission in the SW Fan (see Figure 1). SiO is thought to be associated with shock chemistry and a good tracer of energetic outflows (Ziurys and Friberg 1987; Ziurys et al. 1989; Cherchneff 2006). Interestingly, 183 GHz H_2O masers also trace the clumps in the Fan (Richards 2017). Shock formation of PN also may account for its presence in Cloudlets I-IV. The cloudlets are likely to have been generated in the same event that created the S and SW structures, as they lie about the same distance from the star. Extinction has obscured their detection by HST, similar to the ALMA clumps also to the east of the star (Humphreys et al. 2024).

It is unusual, however, for PN to form in the absence of PO. Almost all shock models of phosphorus chemistry create PO and PN together with abundances within an order of magnitude (e.g., Aota and Aikawa 2012; Lefloch et al. 2016; Jiménez-Serra et al. 2018). It should be noted that some models are for different scenarios than those occurring in VY CMa (cloud condensation, C-shocks, pulsating shocks, etc.), but still offer insight. Both Aota and Aikawa (2012) and Lefloch et al. (2016) found that the PO/PN ratio was sensitive to the nitrogen abundance, enhancements of this element caused PN to be significantly more abundant than PO, especially if the chemical time scales were short (∼100–200 yr). A nitrogen-rich environment could exist in the VY CMa clumps if they contained material dredged up from the H-burning shell. Evidence for N enhancement would be a low ^{12}C/^{13}C ratio (Audouze et al. 1973). Estimates of this ratio in the SW Fan based on HCN suggest ^{12}C/^{13}C ∼ 7. Alternatively, N enrichment could result from grain destruction and liberation of condensed ammonia (Lefloch et al. 2016), but NH_3 is primarily in the gas phase in these regions (Wong et al. 2018). The strong correlation between PN and NS, and the presence of HCN in

Table 1
Line Parameters for PN and PO in VY CMa

Transition	Feature	α (h:m:s)	δ (deg; arcmin; arcsec)	$V_{\rm LSR}$ (km s^{-1})	Peak Intensity (K)	$\Delta V_{1/2}$ (km s^{-1})	HST Features
PN[a]	Spherical	07:22:58.329	−25.46.02.948	20.9 ± 1.4	18.2 ± 0.1	22.3 ± 4.2	…
$J = 5 \rightarrow 4$	SW Fan	07:22:58.289	−25.46.03.879	−4.5 ± 1.4	1.8 ± 0.1	44.1 ± 4.2	…
	...	...	...	10.4 ± 1.4	...	...	S knot B
	...	...	...	20.4 ± 2.8	...	...	SW knot A
	...	...	...	~28	...	...	…
	...	...	...	37.9 ± 4.2	...	...	SW knot *G* *S* knot *E*1 *S* knot *E*2
	Cloudlet I	07:22:58.444	−25.46.02.956	−6.8 ± 2.8	1.4 ± 0.3	9.9 ± 2.8	…
	Cloudlet II	07:22:58.442	−25.46.01.335	−4.5 ± 4.2	1.6 ± 0.3	3.8 ± 4.2	…
	Cloudlet III	07:22:58.329	−25.46.01.666	−3.9 ± 2.8	1.9 ± 0.2	8.8 ± 4.2	…
	...	...	...	35.8 ± 4.2	...	...	...
	Cloudlet IV	07:22:58.246	−25.46.02.451	−3.9 ± 2.8	1.7 ± 0.3	6.5 ± 2.8	…
	...	...	...	44.0 ± 2.8	...	...	...
PO[b]	Spherical	07:22:58.319	−25.46.03.060	14.5 ± 4.2	11.0 ± 0.3	37.0 ± 6.3	…
$J = 5.5 \rightarrow 4.5\ e$	...	...	...	25.6 ± 1.4	...	...	...
PO	Spherical	07:22:58.319	−25.46.03.060	13.1 ± 4.2	11.6 ± 0.3	40.0 ± 6.3	…
$J = 5.5 \rightarrow 4.5\ f$	...	...	...	26.6 ± 1.4	...	...	...

Notes.

[a] Aperture sizes for PN: spherical: 1.″0, SW Fan: 1.″7, Cloudlet I and III: 0.″7, Cloudlet II: 0.″5, Cloudlet IV: 0.″6

[b] Aperture size for PO: spherical: 1.″2; two hyperfine components (see text).

Table 2
Abundances of PN and PO in VY CMa

Molecule	Structure	f [a]
...	Spherical	$(4.4 \pm 1.5) \times 10^{-8}$
...	SW Fan	$(2.6 \pm 0.9) \times 10^{-8}$
PN	Cloudlet I	$\sim 0.4 \times 10^{-8}$
...	Cloudlet II	$\sim 0.2 \times 10^{-8}$
...	Cloudlet III	$\sim 0.5 \times 10^{-8}$
...	Cloudlet IV	$\sim 0.3 \times 10^{-8}$
PO	Spherical	$(1.4 \pm 0.5) \times 10^{-7}$

Note.

[a] Peak abundance relative to H_2.

Cloudlets III and IV (Singh et al. 2023), is compelling evidence for the critical role of nitrogen.

4.3. Phosphorus Production in VY CMa?

Current models predict that approximately 95% of phosphorus originates from SNe, created by neutron-capture processes on ^{29}Si and ^{30}Si within the carbon- and neon-burning shells (Caffau et al. 2011). Simulated SNe-produced phosphorus abundances, however, are too low compared to observations (Cescutti et al. 2012; Nandakumar et al. 2022), and are inconsistent with the recent detections of PO and PN in the outer Galaxy (Koelemay et al. 2023). Alternative sources have been proposed (Karakas 2010).

The abundance of phosphorus contained in molecular form in the spherical source in VY CMa is $\sim 1.8 \times 10^{-7}$. The cosmic abundance of phosphorus, relative to H_2, is 5.2×10^{-7} (Asplund et al. 2009). Therefore, ~35% of the phosphorus could be contained in PO and PN in the spherical outflow. Considering the additional sinks of this element, including atomic forms PI and PII and dust grains, the percentage contained in PO and PN seems high. All other stars studied have 11%–23% (Ziurys et al. 2018). Both molecules may form extremely efficiently in VY CMa, or the star itself is producing phosphorus and ejecting it into the envelope. If VY CMa is producing excess phosphorus, the percentage in PO and PN would be less than 35%.

It is becoming increasingly evident that some massive stars do not become SNe, but quietly collapse into black holes as they sporadically eject matter (e.g., Smartt 2015). Surface activity may account for the asymmetric mass ejections (O'Gorman et al. 2015; Humphreys et al. 2007, 2021). Dredge-up could also be of sufficient magnitude to dip into the carbon-burning shell or the H/He-shell interface. Either region could be producing phosphorus through neutron excess (Karakas 2010). Nonexplosive hypergiants, such as VY CMa, may therefore play a pivotal role in generating phosphorus in the ISM.

5. Conclusion

Being an important biogenic element, there is considerable interest in the chemistry of phosphorus-bearing molecules in the ISM. Our high-fidelity ALMA images of VY CMa have produced the first detailed picture of PO and PN in a circumstellar envelope. While these images demonstrate that both molecules are produced by LTE chemistry near the star, and then disappear due to condensation into dust grains, shocks and an apparent excess of nitrogen create additional PN in more extended regions (SW Clump and cloudlets) where PO is strikingly absent. This rare finding is predicted by shock models for short timescales; the association of PN with the HST dust S/SW knots confirms a 200–300 yr timeline. PN and NS are also found to trace new ejected structures to the N, W, and E of VY CMa, which were not seen in HST dust images but add insight into recent mass loss events. Finally, both PO and PN were found to have an unusually high abundance near the star, suggesting that VY CMa may be ejecting excess phosphorus.

Acknowledgments

This research is supported by NSF grants AST-1907910 and AST-2307305, and NASA grants 80NSSC18K0584 (Emerging Worlds) and 80NSSC21K0593 for the program "Alien Earths." The following data were used: ADS/JAO.ALMA#2021.1.01054. S. ALMA is a partnership of ESO, NSF, and NINS, with NRC, MOST, ASIAA, and KASI, in cooperation with the Republic of Chile. The Joint ALMA Observatory is operated by ESO, AUI/NRAO, and NAOJ. NRAO is a facility of the NSF operated under cooperative agreement by Associated Universities, Inc.

ORCID iDs

R. Ravi https://orcid.org/0000-0002-9204-6270
A. P. Singh https://orcid.org/0000-0002-5419-183X
A. M. S. Richards https://orcid.org/0000-0002-3880-2450
R. M. Humphreys https://orcid.org/0000-0003-1720-9807
L. Decin https://orcid.org/0000-0002-5342-8612
L. M. Ziurys https://orcid.org/0000-0002-1805-3886

References

Adande, G. R., Edwards, J. L., & Ziurys, L. M. 2013, ApJ, 778, 22
Agúndez, M., Cernicharo, J., & Guélin, M. 2007, ApJL, 662, L91
Aota, T., & Aikawa, Y. 2012, ApJ, 761, 74
Asplund, M., Grevesse, N., Sauval, A. J., & Scott, P. 2009, ARA&A, 47, 481
Audouze, J., Truran, J. W., & Zimmerman, B. A. 1973, ApJ, 184, 493
Bernal, J. J., Koelemay, L. A., & Ziurys, L. M. 2021, ApJ, 906, 55
Caffau, E., Bonifacio, P., Faraggiana, R., & Steffen, M. 2011, A&A, 532, A98
Cescutti, G., Matteucci, F., Caffau, E., & François, P. 2012, A&A, 540, A33
Cherchneff, I. 2006, A&A, 456, 1001
Decin, L., Hony, S., Koter, A. D., et al. 2006, A&A, 456, 549
De Beck, E., Kamiński, T., Patel, N. A., et al. 2013, A&A, 558, 9
Dinh-V-Trung, Bao, N. T.-T., Tien, P. M., et al. 2022, AJ, 164, 219
Fontani, F., Rivilla, V. M., van der Tak, F. F.-S., et al. 2019, MNRAS, 489, 4530
Glassgold, A. E. 1996, ARA&A, 34, 241
Hinkel, N. R., Hartnett, H. E., & Young, P. A. 2020, ApJL, 900, L38
Humphreys, R. M., Davidson, K., Richards, A. M.-S., et al. 2021, AJ, 161, 98
Humphreys, R. M., Helton, L. A., & Jones, T. J. 2007, AJ, 133, 2716
Humphreys, R. M., Richards, A. M.-S., Davidson, K., et al. 2024, AJ, 167, 94
Jiménez-Serra, I., Viti, S., Quénard, D., & Holdship, J. 2018, ApJ, 862, 128
Kamiński, T., Gottlieb, C. A., Young, K. H., Menten, K. M., & Patel, N. A. 2013, ApJS, 209, 38
Karakas, A. I. 2010, MNRAS, 403, 1413
Koelemay, L. A., Burton, M. A., Singh, A. P., et al. 2022, ApJL, 940, L11
Koelemay, L. A., Gold, K. R., & Ziurys, L. M. 2023, Natur, 623, 292
Lefloch, B., Vastel, C., Viti, S., et al. 2016, MNRAS, 462, 3937
Lodders, K. 2004, JPCRD, 33, 357
Lodders, K., & Fegley, B. 1999, IAUS, 191, 279
Maas, Z. G., Hawkins, K., Hinkel, N. R., et al. 2022, AJ, 164, 61
Milam, S. N., Halfen, D. T., Tenenbaum, E. D., et al. 2008, ApJ, 684, 618
Nandakumar, G., Ryde, N., Montelius, M., et al. 2022, A&A, 668, A88
O'Gorman, E., Vlemmings, W., Richards, A. M.-S., et al. 2015, A&A, 573, L1
Richards, A. 2017, in Getting Ready for ALMA Band 5 - Synergy with APEX/SEPIA (Garching: ESO)
Rivilla, V. M., Drozdovskaya, M. N., Altwegg, K., et al. 2020, MNRAS, 492, 1180
Roederer, I. U., Jacobson, H. R., Thanathibodee, T., Frebel, A., & Toller, E. 2014, ApJ, 797, 69
Shenoy, D., Humphreys, R. M., Jones, T. J., et al. 2016, AJ, 151, 51
Singh, A. P., Edwards, J. L., Humphreys, R. M., & Ziurys, L. M. 2021, ApJL, 920, L38
Singh, A. P., Edwards, J. L., & Ziurys, L. M. 2022, AJ, 164, 230
Singh, A. P., Richards, A. M.-S., Humphreys, R. M., Decin, L., & Ziurys, L. M. 2023, ApJL, 954, L1
Smartt, S. J. 2015, PASA, 32, e016
Tenenbaum, E. D., Dodd, J. L., Milam, S. N., Woolf, N. J., & Ziurys, L. M. 2010, ApJS, 190, 348
Tenenbaum, E. D., Woolf, N. J., & Ziurys, L. M. 2007, ApJ, 666, L29
Tsuji, T. 1973, A&A, 23, 411
Wittkowski, M., Hauschildt, P. H., Arroyo-Torres, B., & Marcaide, J. M. 2012, A&A, 540, L12
Wong, K. T., Menten, K. M., Kamiński, T., et al. 2018, A&A, 612, A48
Ziurys, L. M. 1987, ApJ, 321, L81
Ziurys, L. M. 2024, ARPC, 75, 307
Ziurys, L. M., & Friberg, P. 1987, ApJ, 314, L49
Ziurys, L. M., Friberg, P., & Irvine, W. M. 1989, ApJ, 343, 201
Ziurys, L. M., Halfen, D. T., Geppert, W., & Aikawa, Y. 2016, AsBio, 16, 997
Ziurys, L. M., Milam, S. N., Apponi, A. J., & Woolf, N. J. 2007, Natur, 447, 1094
Ziurys, L. M., Schmidt, D. R., & Bernal, J. J. 2018, ApJ, 856, 169
Zubko, V., Li, D., Lim, T., Feuchtgruber, H., & Harwitt, M. 2004, ApJ, 610, 427